Pharm Res (2012) 29:2534–2542
DOI 10.1007/s11095-012-0784-7

RESEARCH PAPER

Physiologically Based Pharmacokinetic Model for Composite Nanodevices: Effect of Charge and Size on *In Vivo* Disposition

Donald E. Mager • Vidhi Mody • Chao Xu • Alan Forrest • Wojciech G. Lesniak • Shraddha S. Nigavekar • Muhammed T. Kariapper • Leah Minc • Mohamed K. Khan • Lajos P. Balogh

Received: 29 February 2012 / Accepted: 14 May 2012 / Published online: 12 June 2012

ABSTRACT

Purpose To characterize temporal exposure and elimination of 5 gold/dendrimer composite nanodevices (CNDs) (5 nm positive, negative, and neutral, 11 nm negative, 22 nm positive) in mice using a physiologically based mathematical model.

Methods 400 ug of CNDs is injected intravenously to mice bearing melanoma cell lines. Gold content is determined from plasma and tissue samples using neutron activation analysis. A physiologically based pharmacokinetic (PBPK) model is developed for 5 nm positive, negative, and neutral and 11 nm negative nanoparticles and extrapolated to 22 nm positive particles. A global sensitivity analysis is performed for estimated model parameters.

Results Negative and neutral particles exhibited similar distribution profiles. Unique model parameter estimates and distribution profiles explain similarities and differences relative to positive particles. The model also explains mechanisms of elimination by kidney and reticuloendothelial uptake in liver and spleen, which varies with particle size and charge.

Conclusion Since the PBPK model can capture the diverse temporal profiles of non-targeted nanoparticles, we propose that when specific binding ligands are lacking, size and charge of nanodevices govern most of their *in vivo* interactions.

KEY WORDS composite nanodevices · gold · PBPK model · reticuloendothelial uptake · sensitivity analysis

INTRODUCTION

Pharmacokinetic models have been developed describing how small molecules and large biomacromolecules distribute throughout the body based on chemical and biologic parameters. Steric, electronic and hydrophobic parameters influence biodistribution. Small particles are typically filtered out by the kidney, whereas large particles are removed by the liver and reticuloendothelial system (RES). Research on liposomal delivery systems provides insight into these basic mechanisms of disposition (1). In the field of nanomedicine, however, empiricism is used for each nanoparticle. Models must be developed to permit rational nanodevice design and biodisposition prediction for nanomedicine to advance.

Composite nanodevices (CNDs) are hybrid nanoparticles composed of organic and inorganic chemical

Electronic supplementary material The online version of this article (doi:10.1007/s11095-012-0784-7) contains supplementary material, which is available to authorized users.

D. E. Mager • V. Mody • C. Xu
Dept. of Pharmaceutical Sciences, University at Buffalo SUNY
Buffalo, New York 14260, USA

A. Forrest
Dept. of Pharmacy Practice, University at Buffalo SUNY
Buffalo, New York 14260, USA

W. G. Lesniak • S. S. Nigavekar • M. T. Kariapper • M. K. Khan • L. P. Balogh
NanoBiotechnology Center at RPCI, Dept. of Radiation Medicine
Roswell Park Cancer Institute
Buffalo, New York 14263, USA

L. Minc
Radiation Center Oregon State University
Corvallis, Oregon, USA

M. K. Khan (✉)
Dept. of Radiation Oncology, British Columbia Cancer Agency (BCCA)
Vancouver Centre
600 West 10th Ave.
Vancouver, BC V5Z4E6, Canada
e-mail: Mkhan4@bccancer.bc.ca

entities. The inorganic components are entrapped and uniformly dispersed in organic dendrimer host templates by reactive encapsulation (2,3). They are used for the purpose of imaging (3,4), therapy (3), catalysis (5) and labeling of cells and tissues (2). Metals like Au, Gd, and Ag are used as inorganic guest domains (2,6). Organic domains are dendrimers, which are polymeric, symmetrical and spherical monodisperse macromolecules. They are made up of several units of monomers emanating from the central core and forming a tree-like, branched, and flexible structure that can topologically trap guest atoms, molecules and their clusters (7,8). Poly(amidoamine) (PAMAM) dendrimers with an ethylene diamine core, are most commonly used templates for CNDs due to their biocompatibility, low immunogenicity and structural stability (2,8,9). The dendrimers are classified based upon the number of branched layers, often termed as generations (6).

Hydrophobic, electronic and steric properties of molecules are critically important for their *in vivo* distribution (10). The electronic characteristics are determined by the sign and total charge of the terminal surface functional groups (positive, negative and neutral), which in turn, is dependent on its chemical composition and pH (8,9). The steric properties of CNDs are influenced by size, shape and 3-D conformation and with an increase in generation; there is an increase in size[4]. Furthermore, a PAMAM CND is hydrophilic in nature. Nonetheless, these factors can vary to a large extent based on chemical composition, shape and pH, which largely affects their pharmacokinetic characteristics and targeting (11,12). Therefore, the *in vivo* temporal disposition of CND is complex as compared to small molecules, peptides and antibodies (13). Being hybrid particles, they possess properties of both organic and inorganic components due to which their biodistribution vary largely as compared to simple dendritic nanoparticles (8). It is therefore important to study the pharmacokinetics of CNDs separately and understand the basic determinants that govern their clearance and biodistribution, which will aid in optimization of physicochemical properties, elimination of toxicity and interpretation of exposure-response relationships (9). Whole body physiologically-based pharmacokinetic (PBPK) models mimic the anatomical structure and physiological pathways of the organism that control the time-course of a molecule in plasma and tissues. It incorporates body tissues and fluid compartments which are connected by organ blood flows. Within each tissue, kinetic processes like diffusion, membrane permeability, protein binding, transport kinetics and tissue metabolism can be included based on species-specific and compound-specific input parameters (14). The purpose of this study is to (a) establish a mechanistic PBPK model to describe the *in vivo* behavior of five PAMAM CNDs: 5 nm negative, 5 nm positive, 5 nm neutral, 11 nm negative, and 22 nm positive particles, with entrapped colloidal gold (Au^0) in mice bearing B16F10 melanoma xenografts, and (b) evaluate the effect of size and charge that influence their physiological processes. Based on the model (Fig. 1a,b), we are able to hypothesize the distribution and possible elimination mechanisms for CNDs with respect to their size and charge. We further show that with an increase in size, renal clearance of CNDs decreases, whereas liver and spleen uptake increases. Positively charged particles have greater accumulation in most of the tissues, whereas there is little difference in the disposition of negatively and neutrally charged particles.

MATERIALS AND METHODS

Synthesis of PAMAM Composite Nanodevices

The Au PAMAM dendrimers were synthesized and characterized as reported previously by Balogh and colleagues (8). The positive surface dendrimers had a primary amine groups with a zeta potential +20 mV. The negative surface dendrimers had sodium carboxylate groups with zeta potential −20 mV. The neutral surface dendrimers had acetamide groups and zeta potential of +2.5 mV. The 5 nm particles with negative and neutral charges are generation 4.5 dendrimers and with positive charges are generation 5 dendrimers.

Animal Studies with Tumor Cell Lines

Animal studies were approved by the IACUC and conducted at the animal facility in the University of Michigan Medical Center (Ann Arbor, MI), and adhered to the *Guide for the Care and Use of Laboratory Animals* (NIH publication no. 85-23, revised in 1985). Isogenic B16F10 melanoma cells

Fig. 1 Physiologically-based pharmacokinetic model and temporal profiles of composite nanodevices. (**a**) Schematic PBPK model containing a single blood and nine tissue compartments connected by organ blood flows and each tissue having a specific volume and fractional vascular space. The clearance mechanism is denoted by a renal clearance between kidney and urine compartments and a first-order rate constant indicating biliary excretion between liver and fecal compartments. (**b**) Each tissue is further divided into vascular and extravascular (interstitial) subcompartments with passive permeability or unidirectional uptake between them. (**c**) Temporal profiles of CND concentrations in all the tissues used to develop the model. The circles represent observed data and solid lines represent model predictions after co-modeling four datasets, with colors red, blue, black and green for 5 nm negative, 5 nm neutral, 5 nm positive and 11 nm negative CND respectively. The urine and fecal graphs represent temporal profiles for the cumulative amount of CNDs.

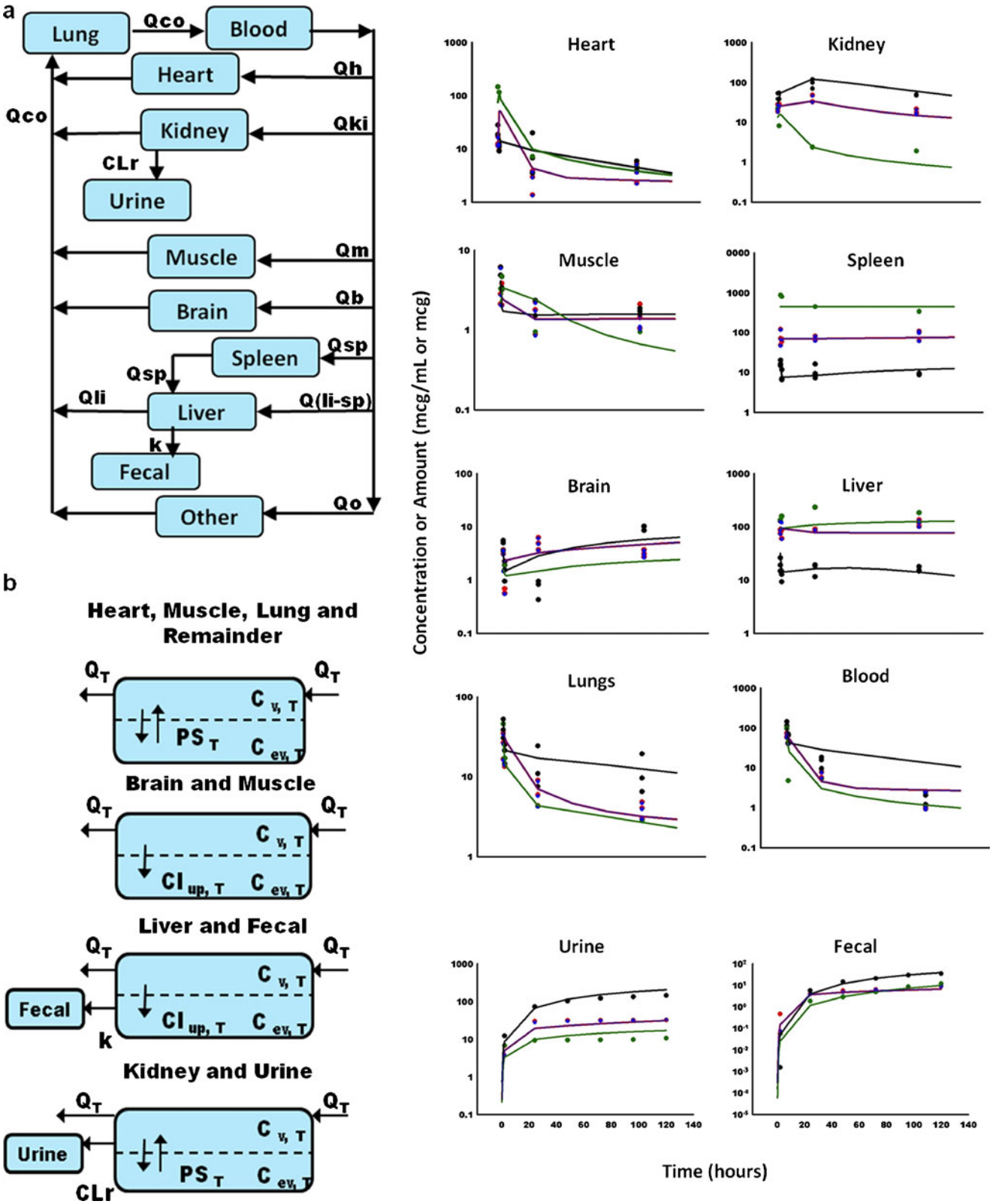

were freshly isolated from carrier mice (11), and 10^6 cells were injected subcutaneously into the dorsal surface of 8–10 week old male C57BL/6J mice (Jackson Labs, Bar Harbor, ME). Tumors were allowed to reach a minimum size of 500 mm^3. A solution of nanocomposites was prepared in PBS (Dulbecco's phosphate-buffered saline, Sigma-

Aldrich, St Louis, MO) with a pH of 7.2. 400 μg (16 mg/kg) of this solution was injected in three tumor-bearing mice intravenously via tail vein injection. Blood samples were collected via cardiac puncture at times 5 min, 1 h, 1 day and 4 days post- injection. The mice were euthanized and the organs (lung, heart, liver, kidney, spleen, pancreas, muscle, tumor and brain) were harvested and weighed to obtain wet weight of the tissues. The samples were taken in triplicates for 5 nm nanocomposites and as single samples for 11 nm and 22 nm nanocomposites.

Determination of Au Content

Au content in the CND and tissue samples were determined by direct neutron irradiation using instrumental neutron activation analysis and used to quantify the concentrations of CND as previously described by Balogh and colleagues (8). The mean Au content was found to be within 0.01% of a certified value, and mean error was less than 2% over a series of 90 irradiations, indicating high accuracy and precision. The limit of detection was 10 ng/ml or 2.5 ng of Au (8).

Excretion Analysis

Urine and fecal samples were collected at times 2 h, 1, 2, 3, 4 and 5 days post-injection using collection tubes from 5 mice housed in each metabolic rodent cage. For 22 nm nanodevices, samples were only collected up to 4 days post-injection. These samples were lyophilized and Au content was quantified as described above.

Model Development

A physiologically-based pharmacokinetic model was developed to determine the *in vivo* disposition of CNDs in mice (Fig. 1a). The model consists of a single blood and nine tissue compartments that are connected by blood flows. A 'remainder' compartment is included as an additional compartment to represent the rest of the body not specifically identified in the model structure. Each compartment, except urine and fecal, is subdivided into vascular and extravascular sub-compartments and a permeability rate-limited tissue model is assumed at the capillary membrane (Fig. 1b). For heart, muscle, lungs, kidney and remainder compartments, a passive permeability mechanism of transport is assumed between the vascular and extravascular sub-compartments since no prolonged accumulation of CND was observed in these tissues. This transport mechanism is represented by a reversible permeability-surface area coefficient term (PS) and a partition coefficient (R). Brain, spleen and liver show significant accumulation in their distribution profiles, hence they are assumed to transfer the nanodevices by a unidirectional flow between the sub-compartments. The differential equations for these tissues are parameterized by an uptake clearance term (CLup). A renal clearance (CLr) is considered, which acts on the vascular compartment of the kidney to the urine compartment. Biliary excretion is indicated by a first order elimination rate constant (k) from extravascular compartment of liver to a fecal compartment, which represents the transport of CND from liver to gut via bile flow.

The physiological values of each organ (blood flow rates, organ weights and fraction of vascular spaces) in mouse were obtained from literature (Supplementary Table S1) (15,16). The sums of the blood flows and volumes were subtracted from the cardiac output and total body weight to calculate parameters associated with the remainder compartment. They are fixed in the model, except for the fraction of vascular space in the remainder compartment, which was estimated. Unknown model parameters like PS, CLup, R, CLr and k for the tissues were estimated by using a semi-PBPK modeling approach in which a simple two compartment model for blood kinetics was fixed and each tissue compartment was fitted individually. These estimates served as initial parameter estimates for the whole body PBPK model. The initial estimates for fractional uptake in liver, spleen and lungs were calculated from the concentrations at 5 min post-injection in these organs. A complete set of differential equations used to characterize the model is given in the Appendix. Unknown model parameters were estimated from fitting the model

Table I Abbreviations of the Parameters Used in the PBPK Model of Composite Nanodevices

Abbreviations	Parameter
R_T	Tissue to blood partition coefficient for the tissue
PS_T	Permeability surface area coefficient of the tissue (ml/hr)
$CL_{up,T}$	Uptake clearance between vascular and extravascular sub-compartments of the tissue (ml/hr)
fsp	Initial fractional uptake in spleen
fli	Initial fractional uptake in liver
fvo	Vascular fraction of remainder compartment
k	First order elimination rate constant from liver to fecal compartment (1/hr)
CL_r	Renal clearance (ml/hr)
$V_{v,T}$	Vascular volume of the tissue (ml)
$V_{ev,T}$	Extravascular volume of the tissue (ml)
Q_T	Blood flow in the tissue (ml/hr)
$C_{v,T}$	Concentration of CNDs in the vascular part of tissue (μg/ml)
$C_{ev,T}$	Concentration of CNDs in the extravascular part of tissue (μg/ml)

The subscripts ki, sp, li, lu, bl, u, f and co are for kidney, spleen, liver, lungs, blood, urine, fecal and cardiac output respectively

(naïve-pooling) using a maximum likelihood algorithm in ADAPT 5 (BMSR, Los Angeles, CA).

Model Qualification

Concentration-time data for the 22 nm positive CNDs were used for the purpose of model qualification. Estimation of initial parameters from a semi-PBPK approach (see "Methods") was not feasible, due to the sparse nature of the data, especially in the blood. Therefore, model parameters were approximately projected from the final estimated parameters obtained after co-modeling, by considering fold-change in terms based on size and charge effects (Supplementary Table S2). High concentrations of these particles were deposited in lungs, indicating that larger particles can be cleared by RES uptake of the alveolar macrophages in lungs, independent of their charge. The structural model is outlined in Methods, and an additional parameter of initial fractional uptake in lungs was included. Simulations were conducted in Berkeley Madonna (v8.0.1, University of California, Berkeley, CA) using this model and the initial projected parameters with the Runge Kutta 4 method. Model parameters were then manually optimized to obtain the best-simulated output. The model produced biased simulation results for tissues like lung, kidney and heart (Supplementary Figure), clearly indicating the need of more data to elucidate the underlying mechanisms and generate initial parameters. The model thus cannot be used for extrapolation to larger particles.

Sensitivity Analysis

Sensitivity analysis of the final PBPK model was conducted using the MATLAB toolbox PottersWheel 2.0.59 (17). The model was simulated 1000 times and the built-in 3-D sensitivity analysis method implemented in PottersWheel was applied, which takes into consideration the mean concentrations of all outcomes for all parameters. The parameters in the model were varied by 20% of their nominal estimated values, and normalized sensitivity indices were calculated for each parameter in each sub-compartment.

RESULTS

Distinct tissue and blood distribution profiles were observed for all four nanodevices (Fig. 1c), with high concentrations in

Table II Estimated Pharmacokinetic Model Parameters of CNDs in Mice

Parameters	Units	5 nm negative/5 nm neutral		5 nm positive		11 nm negative	
		Estimate	CV%	Estimate	CV%	Estimate	CV%
R lung	NA	1.04	24.2	1.04 [a]		2.19	67.5
R muscle	NA	0.489	37.3	0.489 [a]		0.489 [a]	
R heart	NA	0.919	15.0	0.300	16.2	3.35	29.2
R kidney	NA	5.08	11.8	5.08 [a]		0.669	56.9
R other	NA	5.75	16.8	0.542	17.3	2.8	151
PS lung	ml/hr	2.64E-03	46.7	5.58E-04	74.7	2.64E-03 [a]	
PS heart	ml/hr	0.239	18.7	0.239 [a]		3.29	58
PS muscle	ml/hr	0.0414	25.9	7.22E-03	42.8	0.56	63.5
PS kidney	ml/hr	5.68E-02	33.5	0.242	32.3	0.108	103
PS other	ml/hr	0.394	13.6	6.80	43.6	0.394 [a]	
fsp	%	2.22	14.7	0 (fixed)		16.2	16.1
fli	%	37.04	6.18	0 (fixed)		37.04 [a]	
CL_r	ml/hr	4.12E-02	12.9	0.0801	12.9	0.047	23.9
Cl_{up} spleen	ml/hr	3.14E-03	94.1	6.21E-04	30.3	3.14E-03[a]	
Cl_{up} brain	ml/hr	3.24E-03	14.6	1.16E-03	24.1	3.24E-03[a]	
Cl_{up} liver	ml/hr	9.1E-03	16.9	0.0219	18.3	0.304	70.3
fvo	%			6.48 (fixed) [b]			
k	1/hr	0.14	95.6	0.0194	23.8	1.0E-03	64.7
Slope	NA			0.408 [c] (CV%=5.075)			
Intercept	NA			0.175 [c] (CV%=34.73)			

[a] Shared with 5 nm negative/neutral and hence have the same estimates and CV%

[b] Similar across all 4 datasets and is same as the final parameter estimate when 5 nm negative dataset is modeled individually

[c] Variance = (intercept + slope . Y)^2

all organs within 5 min. Blood and lungs show rapid clearance of nanodevices. In the heart tissue, there is a sudden increase in concentrations 5 min post-injection followed by decreased concentrations at later time points. Conversely, in brain tissue, concentrations initially drop sharply and then gradually increase over several days, maximizing at the last time point. Kidney concentrations peak on Day 1 and then decrease at a very slow rate (Day 4 back at 5 min levels). The concentration levels are higher in 5 nm positive particles and lowest in 11 nm negative particles. In liver and spleen, after an initial decrease between 5 min and 1 h, CNDs continue to accumulate showing no indication of washout kinetics by the end of the study period (4 days). 11 nm negative particles accumulate the most in these organs. Along with the brain compartment, where significant accumulation of nanodevices was observed throughout the study time frame, a unidirectional uptake clearance from vascular to extravascular space was modeled (Fig. 1b). The concentration of nanodevices in heart, muscle and brain does not appear to vary significantly with size and charge (Fig. 1c). In contrast, large disparities in distribution are observed in kidney, spleen, liver and urine compartments. For heart, muscle and lung, which do not exhibit such prolonged accumulation, permeability terms between the vascular and extravascular spaces were introduced together with blood/tissue partition coefficients (Fig. 1b). In tumor tissue, approximately 1–4% of the 5 nm negative and neutral, 1.5–6.6% of the 5 nm positive, and 0.6–1.3% of the 11 nm negative CNDs (relative to dose) distributed into the tumor (data not shown). Given the minor distribution into this tissue and lack of measurements of tumor blood flow, this tissue was excluded from the final model.

The temporal profiles of the four CNDs (5 nm negative, 5 nm positive, 5 nm neutral and 11 nm negative) were co-modeled using the final PBPK model (Fig. 1a,b). The objective of co-modeling was to determine the parameters that can be shared across the four devices, as they remain unaffected by size and/or charge variations. This approach facilitated the reduction in both the number of model parameters and the high standard deviation associated with the initial estimates of the 11 nm negative CND parameters (when modeled separately). The final parameters estimated using the PBPK model are presented in Tables I and II. Since the distribution profiles and initial parameter estimates of the 5 nm negative and neutral particles were similar when modeled individually (data not shown), parameters for these two nanodevices were shared throughout. However, Rlung, Rmuscle, Rkidney and PSheart were shared between 5 nm negative/neutral and 5 nm positive particles and found to be independent of charge. Similarly, Rmuscle, PSlung, PSo, fli, CLupsp and CLupb were found to be unaffected by particle size. These parameters were selected since the estimates and/or profiles for these tissues were similar during individual modeling. The majority of the model parameters after co-modeling are estimated with reasonable precision (Table II).

A global sensitivity analysis was performed to determine how the model system would behave in response to parameter perturbation (18,19). Sensitivity indices were generated, which represent the ratio of change in model output normalized to a parameter value, and are based on the perturbations and variability over the entire set of model parameters simultaneously (20). This includes an autosensitivity function describing the sensitivity in a specific compartment due to the parameters of that compartment, and a cross-sensitivity function, describing the sensitivity in a specific compartment due to the parameters of another compartment (18).

As expected, the autosensitivity tends to be greater than cross-sensitivity for most tissues (Fig. 2). Model outcome is primarily sensitive to fsp and fli, which have a negative impact on all of the included tissues. The 5 nm negative and neutral particles are only sensitive to fli, the 11 nm particles are sensitive to both fsp and fli, and the 5 nm positive particles are insensitive to all of these terms. This finding is in agreement with the hypothesis that RES clearance becomes significant for larger particles and negligible for positive particles. The concentration in the blood compartment is relatively insensitive to all terms except for these two parameters. The model for 11 nm particles is also sensitive to the uptake clearance for liver, which has a negative impact on the concentrations in all tissues. Likewise, renal clearance is also found to be influencing the model output for 5 nm positive devices only. However, the overall sensitivity of the model to all the parameters is found to be lower. This can be attributed to the parallel structure of the model, which can cause dampening of the perturbations as it gets distributed by the closed circulatory flow; to the inputs of all parallel peripheral compartments in the model (18).

DISCUSSION

In the present study, a PBPK model is developed that successfully describes the disposition of composite nanodevices after intravenous administration into mice bearing melanoma cell lines. The model is also able to highlight the important elimination pathways of these particles, that varies based upon its size and charge. From the model results, renal clearance is the major route of elimination for CNDs as reflected in high urinary concentrations in Fig. 1c. The size cutoff for glomerular filtration in the kidney tubules is <5.5 nm diameter (21,22). Therefore, the 5 nm nanoparticles (approx. 26.2 kDa) are easily filtered in the glomerulus and cleared in urine, whereas the 11 nm particles are excreted in lesser quantities. Since the parameter estimates for renal clearance and permeability (PS) in the kidney are 2–4 fold higher for positive particles as compared to the other three devices,

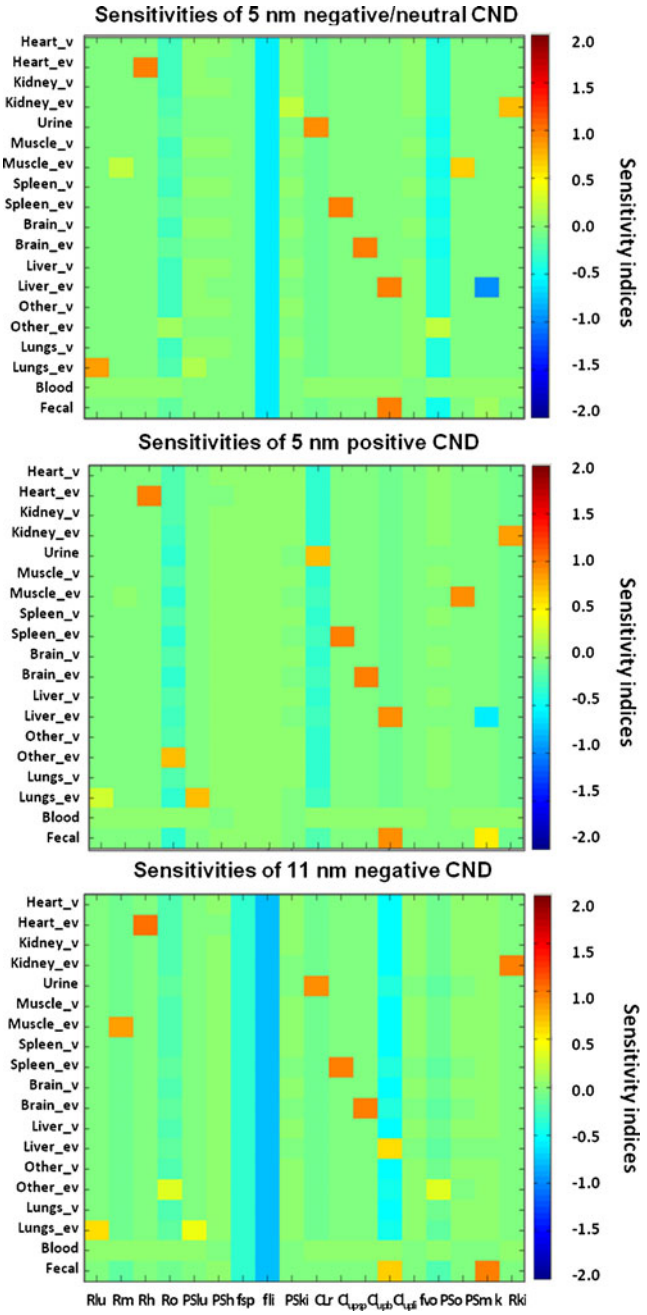

Fig. 2 Sensitivity analysis for the final PBPK model. Sensitivity heat-maps for 5 nm negative, 5 nm neutral, 5 nm positive, and 11 nm negative CNDs generated by the PottersWheel toolbox 2.0.59 in MATLAB. The box on the right side of each plot shows a range of sensitivity indices, the y-axis represents the subcompartments of each tissue in the model, and the x-axis consists of all the estimated parameters of the model. A positive sensitivity index indicates a positive impact and a negative sensitivity index indicates a negative impact of the parameter on the concentrations of CNDs in a specific tissue.

positive particles are eliminated to a larger extent from kidneys. Electrostatic interactions between the negative charge of glomerular basement membranes might account for higher permeability and tissue uptake of positively charged particles; processes which modulate the tight junctions of the glomerular capillary wall (23,24). Although kidney concentrations peak at day 1 and later decrease for the 5 nm particles (with significant accumulation of positive particles in kidney and urine), concentrations of 11 nm particles are lower in both tissues. The 5 nm neutral CNDs are uncharged particles; however, there is no evidence of tubular reabsorption, and their disposition is similar to 5 nm negative particles (25).

For negative and neutral CNDs, significantly high concentrations were observed within 5 min of dosing in liver and spleen. This could result from rapid uptake and clearance by the RES macrophage-lineage cells lining these organs (26). The process of opsonization attaches serum proteins (opsonins) to the CND, increasing susceptibility to phagocytosis and enzymatic degradation by macrophages and eventually eliminating them from the bloodstream (26). For both devices we approximated this process by estimating fractions of dose immediately taken up by these two organs just after injection (fsp and fli). Nanoparticle clearance by this phenomenon is largely dependent on size, charge and composition. Surface negative or neutral charge increases opsonization and clearance by activating a classical pathway of the complement system (1). Positive surface charge may cause opsonization in human serum but not in rodent serum (27). Therefore, the fractional uptake in liver and spleen was fixed to zero for the 5 nm positive devices in the model, suggesting minimum RES uptake, and reflecting lower tissue concentrations. This may also result in increased availability in other tissues. Particles larger than the renal threshold have a higher tendency to be cleared from the blood by this mechanism (26,28,29). Consequently, high deposition is observed in liver and spleen for 11 nm negative CNDs. The estimate of fractional uptake in spleen is 8-fold higher and the uptake clearance in liver is 30–fold higher for 11 nm negative as compared to 5 nm negative or neutral nanodevices (Table II). These modeling results are comparable to studies with ^{153}Gd labeled PAMAM dendrimers (28,29). Similarly, we also confirm that positive nanoparticles have a greater extent of permeability and cellular uptake as compared to negative nanoparticles (24). Since the 11 nm particles are degraded by liver to a greater extent, fewer particles would enter the biliary circulation into the fecal tissue. The biliary excretion is represented by a first-order rate constant (k) from the extravascular part of liver to the fecal compartment. The lower parameter estimate for k, also suggests that 11 nm negative CNDs are excreted through bile to a lesser extent as compared to the 5 nm devices. This observation is contrary to the literature, wherein biliary excretion is greater for large molecular

size and weight compounds (30). However, as a drawback, CNDs continue to accumulate in these two tissues showing no indication of washout kinetics by the end of the study period of 4 days.

Although the concentration profiles in brain and muscle are similar for 5 nm negative, neutral and positive particles, the estimated parameters for the positive CNDs are much lower (6-fold for PS muscle and 3-fold for uptake clearance in brain). This is because less permeable organs, like brain and muscle, exhibit greater resistance for tissue uptake of positive particles.

CONCLUSIONS

We have successfully identified the unique distributive properties associated with charged composite nanodevices using a physiologically-based model. This represents a first step toward identifying the complex contributions of structural characteristics (size, charge and structural composition) and developing mechanism-based equations for the *a priori* prediction of the *in vivo* disposition of nanoparticles and multifunctional nanodevices. Charge- and size-dependent interactions between these particles and biological matrices are critically important for the development and optimization of these particles. In this study, the accumulation of nanodevices was evaluated as a function of its size and charge, without the use of a targeting moiety.

A major limitation of the current study is the lack of data and sampling points in the terminal elimination phase. The assumption of unidirectional uptake in tissues like brain, spleen and liver is not very likely and they may undergo a reversible uptake from extravascular to the vascular part of the tissue. The lack of sufficient elimination phase data prohibited the inclusion of a bidirectional flux in these tissues suggesting a relatively short collection interval. This limitation also influenced the prediction of distribution profiles for the 22 nm nanodevices. Information on protein and receptor binding is also missing, which might be important since dendrimers exhibit a tendency to undergo receptor mediated endocytosis, which can further explain its in-depth tissue transport kinetics (31). The current PBPK model does not incorporate convective flow due to lymphatics, which is thought to have an important role in distribution of larger particles due to the presence of large pores in lymph vessels. Attempts to fit the lymph flow and vascular reflection coeffecients to represent convection in each tissues were not successful due to high correlations between the parameters (data not shown) (32).

Our modeling approach is a prototype of whole body pharmacokinetic assessments in the area of nanomedicine, and this basic model can serve as a starting point for further exploring the *in vivo* disposition of such systems. Measurements of pharamacodynamic endpoints in tumor tissue may also be useful to study the exposure-response relationships of CNDs in the target tumor tissue. Furthermore, we hypothesize that the integration of PBPK modeling with quantitative structure–property relationships will eventually reveal the dominant structures and processes controlling the spatio-temporal exposure profiles of nanoparticles.

ACKNOWLEDGMENTS AND DISCLOSURES

This study was supported in part by NIH (5R01 CA104479), DOD (DAMD17-03-1-0018), and DOE (DE-PS01-00NE22740), and also Eli Lilly and Company predoctoral fellowship (to C.X.), and a new investigator grant from the American Association of Pharmaceutical Sciences (to D.E.M).

REFERENCES

1. Gabizon A, Papahadjopoulos D. Liposome formulations with prolonged circulation time in blood and enhanced uptake by tumors. Proc Natl Acad Sci. 1988;85(18):6949–53.
2. Lesniak W, Bielinska AU, Sun K, Janczak KW, Shi X, Baker JR, *et al.* Silver/dendrimer nanocomposites as biomarkers: fabrication, characterization, *in vitro* toxicity, and intracellular detection. Nano Letters. 2005;5(11):2123–30.
3. Khan MK, Minc LD, Nigavekar SS, Kariapper MST, Nair BM, Schipper M, *et al.* Fabrication of 198Au0 radioactive composite nanodevices and their use for nanobrachytherapy. Nanomed Nanotechnol Biol Med. 2008;4(1):57–69.
4. Shi X, Wang S, Meshinchi S, Van Antwerp ME, Bi X, Lee I, *et al.* Dendrimer-entrapped gold nanoparticles as a platform for cancer-cell targeting and imaging. Small. 2007;3(7):1245–52.
5. Crooks RM, Zhao M, Sun L, Chechik V, Yeung LK. Dendrimer-encapsulated metal nanoparticles: synthesis, characterization, and applications to catalysis. Acc Chem Res. 2000;34(3):181–90.
6. Menjoge AR, Kannan RM, Tomalia DA. Dendrimer-based drug and imaging conjugates: design considerations for nanomedical applications. Drug Discov Today. 2010;15(5–6):171–85.
7. Lee CC, MacKay JA, Frechet JMJ, Szoka FC. Designing dendrimers for biological applications. Nat Biotech. 2005;23 (12):1517–26. doi:10.1038/nbt1171.
8. Balogh L, Nigavekar SS, Nair BM, Lesniak W, Zhang C, Sung LY, *et al.* Significant effect of size on the *in vivo* biodistribution of gold composite nanodevices in mouse tumor models. Nanomed Nanotechnol Biol Med. 2007;3(4):281–96.
9. Khan MK, Nigavekar SS, Minc LD, Kariapper MS, Nair BM, Lesniak WG, *et al. In vivo* biodistribution of dendrimers and dendrimer nanocomposites—implications for cancer imaging and therapy. Technol Cancer Res Treat. 2005;4(6):603–13.
10. Mager DE. Quantitative structure-pharmacokinetic/pharmacodynamic relationships. Adv Drug Deliv Rev. 2006;58(12–13):1326–56.
11. Nigavekar S, Sung L, Llanes M, El-Jawahri A, Lawrence T, Becker C, *et al.* 3H dendrimer nanoparticle organ/tumor distribution. Pharm Res. 2004;21(3):476–83.
12. Wijagkanalan W, Kawakami S, Hashida M. Designing dendrimers for drug delivery and imaging: pharmacokinetic considerations. Pharm Res. 2011;28(7):1500–19.

13. Zhou Q, Gallo J. The pharmacokinetic/pharmacodynamic pipeline: translating anticancer drug pharmacology to the clinic. AAPS J. 2011;13(1):111–20.
14. Nestorov I. Whole body pharmacokinetic models. Clin Pharmacokinet. 2003;42(10):883–908.
15. Brown RP, Delp MD, Lindstedt SL, Rhomberg LR, Beliles RP. Physiological parameter values for physiologically based pharmacokinetic models. Toxicol Ind Health. 1997;13(4):407–84.
16. Davies B, Morris T. Physiological parameters in laboratory animals and humans. Pharm Res. 1993;10(7):1093–5.
17. Maiwald T, Timmer J. Dynamical modeling and multi-experiment fitting with PottersWheel. Bioinformatics. 2008;24(18):2037–43.
18. Nestorov IA. Sensitivity analysis of pharmacokinetic and pharmacodynamic systems: I. A structural approach to sensitivity analysis of physiologically based pharmacokinetic models. J Pharmacokinet Pharmacodyn. 1999;27(6):577–96.
19. Fenneteau F, Li J, Nekka F. Assessing drug distribution in tissues expressing P-glycoprotein using physiologically based pharmacokinetic modeling: identification of important model parameters through global sensitivity analysis. J Pharmacokinet Pharmacodyn. 2009;36(6):495–522.
20. Nestorov IA, Aarons LJ, Rowland M. Physiologically based pharmacokinetic modeling of a homologous series of barbiturates in the rat: a sensitivity analysis. J Pharmacokinet Pharmacodyn. 1997;25 (4):413–47.
21. Longmire M, Choyke PL, Kobayashi H. Clearance properties of nano-sized particles and molecules as imaging agents: considerations and caveats. Nanomedicine. 2008;3(5):703–17.
22. Soo Choi H, Liu W, Misra P, Tanaka E, Zimmer JP, Itty Ipe B, *et al.* Renal clearance of quantum dots. Nat Biotech. 2007;25(10):1165–70.
23. Boswell CA, Tesar DB, Mukhyala K, Theil F-P, Fielder PJ, Khawli LA. Effects of charge on antibody tissue distribution and pharmacokinetics. Bioconjugate Chem. 2010;21(12):2153–63.
24. Kim B, Han G, Toley BJ, Kim C-k, Rotello VM, Forbes NS. Tuning payload delivery in tumour cylindroids using gold nanoparticles. Nat Nano. 2010;5(6):465–72.
25. Varma MVS, Feng B, Obach RS, Troutman MD, Chupka J, Miller HR, *et al.* Physicochemical determinants of human renal clearance. J Med Chem. 2009;52(15):4844–52.
26. Owens 3rd DE, Peppas NA. Opsonization, biodistribution, and pharmacokinetics of polymeric nanoparticles. Int J Pharm. 2006;307(1):93–102.
27. Devine DV, Bradley AJ. The complement system in liposome clearance: can complement deposition be inhibited? Adv Drug Deliv Rev. 1998;32(1–2):19–29.
28. Kobayashi H, Kawamoto S, Saga T, Sato N, Hiraga A, Konishi J, *et al.* Micro-MR angiography of normal and intratumoral vessels in mice using dedicated intravascular MR contrast agents with high generation of polyamidoamine dendrimer core: Reference to pharmacokinetic properties of dendrimer-based MR contrast agents. J Magn Reson Imaging. 2001;14(6):705–13.
29. Kobayashi H, Sato N, Hiraga A, Saga T, Nakamoto Y, Ueda H, *et al.* 3D-micro-MR angiography of mice using macromolecular MR contrast agents with polyamidoamine dendrimer core with reference to their pharmacokinetic properties. Magn Reson Med. 2001;45(3):454–60.
30. Hirom PC, Millburn P, Smith RL, Williams RT. Species variations in the threshold molecular-weight factor for the biliary excretion of organic anions. Biochem J. 1972;129(5):1071–7.
31. Kitchens KM, Kolhatkar RB, Swaan PW, Ghandehari H. Endocytosis inhibitors prevent poly(amidoamine) dendrimer internalization and permeability across Caco-2 Cells. Mol Pharm. 2008;5(2):364–9.
32. Covell DG, Barbet J, Holton OD, Black CD, Parker RJ, Weinstein JN. Pharmacokinetics of monoclonal immunoglobulin G1, F(ab')2, and Fab' in mice. Cancer Res. 1986;46(8):3969–78.